Journal of Materials Chemistry A

ROYAL SOCIETY OF CHEMISTRY

PAPER

View Article Online
View Journal | View Issue



Cite this: J. Mater. Chem. A, 2025, 13, 30128

# Revealing complex magnetic interactions in $Fe_2P$-based compounds: a study using Mössbauer spectroscopy and neutron diffraction

Karthika K. Thilakan,[a] Sagar Ghorai,[b] Wei Liu,[b] Lennart Häggström,[c] Fredrik Lindgren,[a] Vladimir Pomjakushin,[d] Premysl Beran,[ef] Oliver Gutfleisch,[b] Peter Svedlindh[gh] and Johan Cedervall *[a]

The magnetic properties of $Fe_{2-2x}Mn_{2x}P_{1-x}Si_x$ ($0 \leq x \leq 0.5$) compounds are studied by neutron diffraction, Mössbauer spectroscopy, and magnetometry. DC magnetization measurements indicate that compounds with $0.2 \leq x \leq 0.5$ undergo a paramagnetic to ferromagnetic transition, with the Curie temperature increasing as $x$ increases. In contrast, compounds with $0 < x \leq 0.15$ show unclear magnetic ordering in DC magnetization measurements, while AC magnetization measurements display frequency-dependent peaks, indicating glassy spin dynamics. For the $x = 0.125$ sample, AC magnetization measurements under applied DC fields suggest that the transition at 150 K corresponds to a complex antiferromagnetic (AFM) structure. Mössbauer spectroscopy reveals four distinct regions of hyperfine interactions for different $x$ values, suggesting extreme sensitivity in the magnetic behaviour with Mn and Si substitutions. For $0 < x < 0.15$, a drop in the magnetic hyperfine field supports the existence of a complex AFM structure. Neutron diffraction on the $x = 0.1$ sample confirms an incommensurate AFM structure with a propagation vector $q_x = 0.2204(4)$, consistent with the Mössbauer and magnetization results.

Received 17th April 2025
Accepted 17th July 2025

DOI: 10.1039/d5ta03047a

rsc.li/materials-a



Johan Cedervall

*Johan Cedervall (PhD 2017) is a researcher in inorganic chemistry at Uppsala University, Sweden where he joined in 2023 after a post-doc at ISIS Neutron and Muon Source, UK. His main research interests are within the fields of sustainable magnetic materials, including permanent magnets and magnetic refrigeration. He has expertise within high temperature synthesis, crystallography (including magnetic structure solution) and neutron scattering, which is used to synthesise novel magnetic materials and evaluate their structural and intrinsic magnetic properties. Cedervall has published ~40 scientific papers and have received research grants from the Swedish Research Council and ÅForsk.*

## 1 Introduction

Magnetocaloric materials have attracted significant interest as a promising alternative to traditional gas compression methods for magnetic refrigeration.[1–4] $Fe_2P$-based compounds are among the most promising candidates for magnetic refrigeration due to their large magnetocaloric effect (MCE) resulting from the first-order magnetic transition (FOMT).[5–9] $Fe_2P$ and its derivatives when substituted with Mn and Si exhibit an intriguing phase diagram, Fig. 1. $Fe_2P$ and $Mn_2P$ adopt a hexagonal $P\bar{6}2m$ structure, while the intermediate compound FeMnP crystallizes in an orthorhombic *Pnma* structure ($Co_2P$-type). Substituting P with Si in $Fe_2P$ gives rise to another orthorhombic structure. However, single-phase compounds corresponding to $Fe_2Si$ and $Mn_2Si$ cannot be synthesized, as they are in a multiphase region. The center of this phase diagram is occupied by $FeMnP_{0.5}Si_{0.5}$, which retains the $Fe_2P$ structure.

[a]Department of Chemistry, Ångström Laboratory, Uppsala University, Box 538, 751 21 Uppsala, Sweden. E-mail: johan.cederall@kemi.uu.se
[b]Institute of Materials Science, Technical University of Darmstadt, 64287 Darmstadt, Germany
[c]Department of Physics and Astronomy, Uppsala University, Box 516, 751 20 Uppsala, Sweden
[d]Laboratory for Neutron Scattering and Imaging, Paul Scherrer Institut, 5232 Villigen, Switzerland
[e]European Spallation Source ESS ERIC, Box 176, 221 00, Lund, Sweden
[f]Nuclear Physics Institute, ASCR, Hlavni 130, 25068 Rez, Czech Republic
[g]Department of Materials Science and Engineering, Uppsala University, Box 35, 751 03 Uppsala, Sweden
[h]WISE – Wallenberg Initiative Materials Science for Sustainability, Department of Materials Science and Engineering, Uppsala University, SE-751 03 Uppsala, Sweden

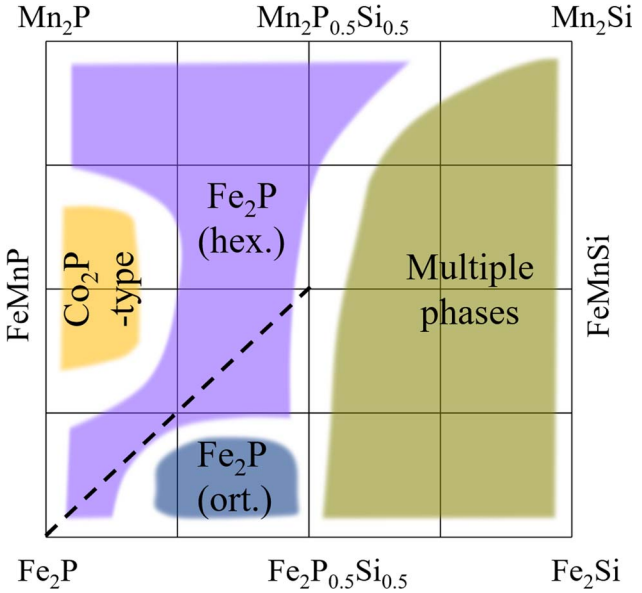


Fig. 1 Quaternary phase diagram of the Fe–Mn–P–Si system. The samples studied in this paper lie on the dotted line.

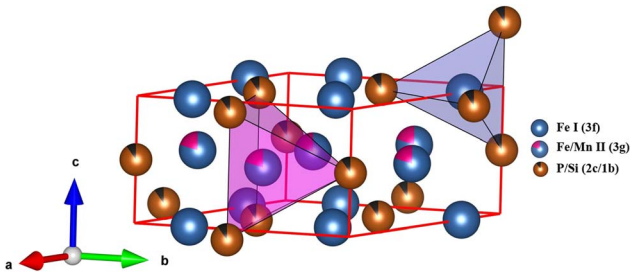


Fig. 2 Coordination polyhedra of the metal atoms: tetrahedral 3f site (represented as blue polyhedron) and pyramidal 3g site (represented as pink polyhedron).

$Fe_2P$-based compounds are particularly intriguing due to their tunable transition temperature, non-toxic and non-critical raw materials, and high isothermal magnetic entropy change.[10] These compounds crystallize in a hexagonal $P\bar{6}2m$ space group with two independent metal sites; tetrahedral 3f and pyramidal 3g sites (Fig. 2). Several studies have shown that Mn preferentially occupies the larger pyramidal 3g site in Mn-substituted compounds of $Fe_2P$.[11–14] The occupation of the non-metal atoms P and Si in the 1c and 2b sites shows no preference in almost all cases. However, XRD refinement and energy calculations of the compound $Fe_{0.6}Mn_{1.4}P_{0.6}Si_{0.4}$ using the Korringa–Kohn–Rostoker Coherent Potential Approximation (KKR-CPA)[15] and the neutron diffraction study of $Fe_{0.70}Mn_{1.25}P_{1-x}Si_x$ ($x$ = 0.45, 0.50, 0.55) by Miao *et al.*[16] suggest that Si atoms preferentially occupy the 2c site. A relation between the Si content and the magnetic hyperfine field at the Fe sites in $Fe_2P_{1-x}Si_x$ compounds has been established using Mössbauer spectroscopy.[17] It was observed that the magnetic hyperfine field at the tetrahedral and pyramidal Fe sites increases with increasing Si content. Another significant result from Mössbauer studies[12,18] is that the magnetic Fe hyperfine field at the tetrahedral 3f site increases considerably from 11.4 T in $Fe_2P$ to 22.8 T in $FeMnP_{0.5}Si_{0.5}$. The magnetic hyperfine field at the 3g pyramidal site cannot be measured in $FeMnP_{0.5}Si_{0.5}$ due to the absence of Fe atoms at this site. However, Fruchart *et al.*[15] measured the hyperfine field at the 3g site for the compound $Fe_{1.4}Mn_{0.6}P_{0.6}Si_{0.4}$ at 84 K as 19.5 T, which can be compared with 17.2 T in $Fe_2P$.[18]

The MCE is quantified by measuring isothermal entropy and adiabatic temperature changes in materials. Large values of these parameters indicate the strong potential of a material for magnetocaloric applications. Although a high isothermal magnetic entropy change is observed in the $(Fe,Mn)_2(P,Si)$ system, considerable thermal hysteresis ($\Delta T_{hys}$ = 35 K) is associated with FOMT.[10] The isothermal entropy change ($\Delta S_{mag}$) of $FeMnP_{0.5}Si_{0.5}$ with an applied magnetic field of 2 T is 16.5 J kg$^{-1}$ K$^{-1}$, making it very competitive with other materials for magnetic cooling applicaitons.[19] Corresponding values for other magnetocaloric materials are 5.2, 18.4, 21.7 and 15 J kg$^{-1}$ K$^{-1}$, for Gd, $Gd_5Si_2Ge_2$, $LaFe_{11.6}Si_{1.4}$ and $Ni_{50.2}Mn_{35.0}In_{14.8}$ (Heusler), respectively.[20] The search for optimal Fe : Mn and P : Si ratios is key to obtaining reduced thermal hysteresis while maintaining the giant magnetocaloric effect in the Fe–Mn–P–Si system. So far, the studies on $(Fe,Mn)_2(P,Si)$ compounds were mainly focused on keeping equal amounts of Fe and Mn.[10,12,21–23] These compounds, which crystallize in the hexagonal $Fe_2P$-type phase, are explored to understand the magnetic interactions behind the physics of magnetic cooling. In $Fe_2P$, the magnetic moments are ferromagnetically ordered along the hexagonal $c$-axis below the transition temperature[7,18] $T_c$ while in $FeMnP_{0.5}Si_{0.5}$ they are aligned along the $a$-axis.[22] However, $FeMnP_{0.75}Si_{0.25}$ shows a complex antiferromagnetic (AFM) ordering.[21] Therefore, it is important to investigate the compositions between $Fe_2P$ and $FeMnP_{0.5}Si_{0.5}$ to understand the stability of the ferromagnetic state (FM) and ultimately to develop improved design guidelines for magnetocaloric materials.

In this work, a series of stoichiometric compounds $Fe_{2-2x}Mn_{2x}P_{1-x}Si_x$ ($0 \leq x \leq 0.5$) were synthesized using the drop synthesis method and studied through neutron diffraction, magnetization measurements, and Mössbauer spectroscopy.

## 2 Methods

### 2.1 Synthesis

Master alloys of $Fe_2P$ and $FeMnP_{0.5}Si_{0.5}$ were prepared from stoichiometric amounts of iron (Leico Industries, purity 99.99+%. Surface oxides were reduced in $H_2$-gas), manganese (Institute of Physics, Polish Academy of Sciences, purity 99.999%), phosphorus (Alfa Aesar, purity 99.999+%) and silicon (Highways International, purity 99.999%) using the drop synthesis method.[24] Intermediate samples of $Fe_{2-2x}Mn_{2x}P_{1-x}Si_x$ were prepared by mixing stoichiometric amounts of the master alloys. All samples were sealed in evacuated silica ampules and annealed at 1370 K for 2 h, followed by heat treatment at 1270 K for 10 days and rapid quenching.

### 2.2 Diffraction

X-ray diffraction experiments were performed using a Bruker D8 Advance operating with Cu K$\alpha$ radiation and equipped with a LynxeyeXE position sensitive detector. Neutron powder

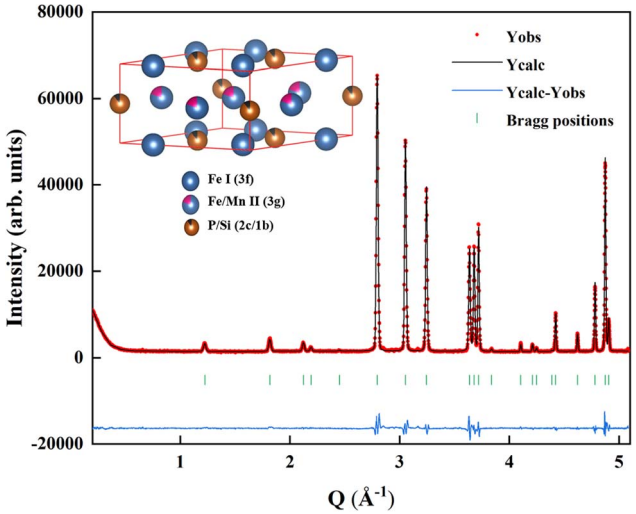


Fig. 3 Neutron diffraction ($\lambda = 2.45$ Å) pattern for $Fe_{1.8}Mn_{0.2}P_{0.9}Si_{0.1}$ at room temperature. The refined structure model is shown as an inset.

diffraction (NPD) was employed using the HRPT instrument[25] at SINQ (PSI, Villigen Switzerland). A Ge monochromator (reflection 400) was used that gives a wavelength of 2.45 Å. All samples were measured in a temperature range of 10 to 300 K.

The obtained diffraction data was analyzed using the Rietveld method[26] implemented in the FullProf software.[27] In the refinements, several structure parameters, including atomic positions, occupancies, and displacement, were allowed to vary. For incommensurate magnetic structures, the magnetic propagation vectors, **k**, were investigated using **k**-search implemented in the FullProf Suite. The obtained **k**-vectors were used as input parameter to find irreducible representations (IR) with the SARAh software.[28] The obtained IRs were later implemented in full-pattern magnetic structure refinements.

### 2.3 Magnetometry

A Quantum Design magnetic property measurement system was used to assess the magnetic properties of samples. The temperature dependent magnetization under field-cooled cooling (FC) and field-cooled warming (FCW) conditions were measured using an applied magnetic field of $\mu_0 H = 10$ mT. Temperature- and frequency-dependent AC susceptibility measurements were performed to study the low-frequency relaxation behavior of the compounds with $0.05 \leq x \leq 0.15$ using an AC magnetic field amplitude of $\mu_0 H_{AC} = 0.4$ mT.

### 2.4 Mössbauer spectroscopy

Mössbauer measurements were carried out on a spectrometer working with a constant acceleration type of vibrator and a $^{57}$CoRh source. The spectra were recorded at low temperatures in an Oxford He-flow cryostat and at high temperatures in a Ricor furnace, respectively. The $Fe_{2-2x}Mn_{2x}P_{1-x}Si_x$-samples were mixed with inert BN and enclosed in sealed kapton pockets. The absorbers formed thus had a sample concentration of ~2–20 mg cm$^{-2}$. Calibration spectra were recorded at 295 K using natural Fe metal foil as a reference absorber. The spectra were folded and fitted using the least square Mössbauer fitting program Recoil to obtain the values of the center shift (CS) *versus* natural α-Fe at 295 K, the electric quadrupole splitting (QS) (in the paramagnetic regime), the electric quadrupole shift ($\varepsilon$) and the magnetic hyperfine field ($B_{hf}$) (in the magnetic

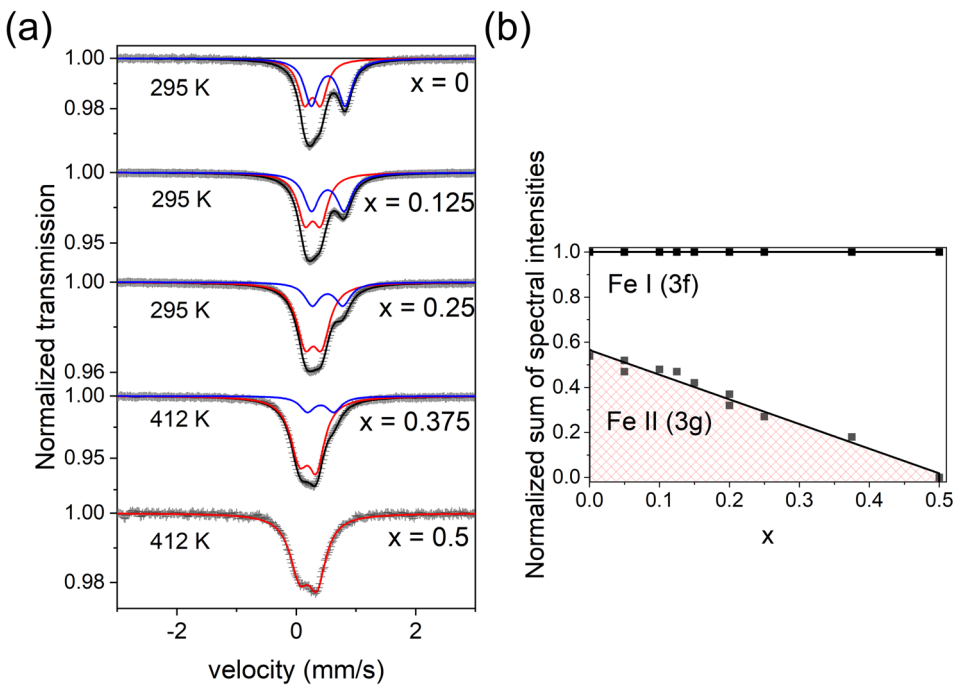


Fig. 4 (a) Mössbauer spectra in the paramagnetic regime for different values of *x*. The red and blue subspectra emanate from Fe(1) at the tetrahedral 3f and Fe(2) at the pyramidal 3g positions, respectively. (b) Normalized sum of spectral intensities of tetrahedral Fe(1) and pyramidal Fe(2) *versus* *x* in $Fe_{2-2x}Mn_{2x}P_{1-x}Si_x$.

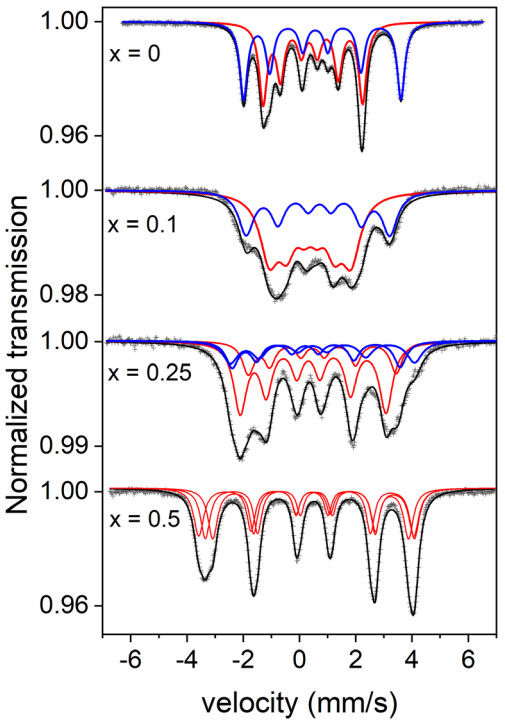


Fig. 5 Mössbauer spectra of $Fe_{2-2x}Mn_{2x}P_{1-x}Si_x$ at 85 K. Blue and red represent Fe at the pyramidal (3g) and tetrahedral (3f) sites, respectively.

regime), the full-width at half maxima ($W$) of the Lorentzian absorption lines and the spectral areas ($A$).

# 3 Results

## 3.1 Phase analysis

All samples are of high purity, with only trace amounts of secondary phases, as shown in Fig. 3 for $x = 0.1$. Structural refinements show that all samples crystallize in the $Fe_2P$-type structure, space group (SG) $P\bar{6}2m$. The evolution of the unit cell parameter, studied using XRD, Fig. S1 in SI, gives a clear trend where $a$ ($c$) increases (decreases) with increasing amount of $x$. This also affects the $c/a$-ratio, which decreases with increasing level of substitution. There is a shift in the unit cell parameters between $x = 0.25$ and 0.375 due to magnetostriction as samples with $x > 0.25$ have $T_C$ above RT. The unit cell parameters for the master alloys ($Fe_2P$ and $FeMnP_{0.5}Si_{0.5}$) are in excellent agreement with the values previously reported, which in combination with the NPD results indicate that the substitutions have been successful. The structure refinement to the NPD data confirms that Mn preferably occupies the pyramidal 3g position even in low concentrations, shown as an inset in Fig. 3, in agreement with previous findings.[16,21,22,29] Varying the Fe and Mn occupancies were tested in the refinements, but as it did not improve the refined model they were left in their nominal compositions.

## 3.2 Mössbauer spectroscopy

**3.2.1 Paramagnetic regime.** In Fig. 4 the Mössbauer spectra in the paramagnetic regime are presented along with the spectral areas for the two crystallographic sites. The area of Fe(2) at pyramidal 3g sites decreases with increasing $x$ and at $x = 0.5$, ($FeMnP_{0.5}Si_{0.5}$), all contributions to the pattern come from Fe(1) at tetrahedral 3f sites. This confirms the findings from NPD that Mn atoms are solely located at the pyramidal 3g site all through the substitution series. The fitted results using one Mössbauer pattern each for Fe(1) and Fe(2) are presented in Table S1.

A detailed study of the Fe(1) subspectrum for $x = 0.5$ and $x = 0.375$ shows some asymmetric doublet behavior that is caused by an atomic disorder in the near surroundings of Fe(1) at the tetrahedral 3f site. It is expected since the four nearest neighbour (nn) atoms P or Si can vary. The nn to the 3f site is two P or Si atoms at the 1b site and two P or Si atoms at the 2c site. Each surrounding would give slightly different Mössbauer subspectra, which may explain the asymmetry and broadening in the spectrum as shown in Fig. 4. It has been argued that Si preferentially occupies the 2c-site,[15] however, by analysing the Mössbauer hyperfine spectra of $Fe_2P_{1-x}S_x$ with $0.10 \leq x \leq 0.16$ the P/Si substitution is shown to be almost random.[17] However, the resolution in the present spectra in the paramagnetic regime is too low to resolve any preference of the P/Si occupation.

**3.2.2 Magnetic regime.** The hyperfine parameters are affected differently due to the various amounts of P, Si, Mn and Fe atoms around each Fe metallic site. The spectra have therefore been fitted with 2 to 4 sextet patterns depending on the $x$-value (Fig. 5). In the fitting, all subspectra representing Fe at the 3f site have the constraint of having the same central shift CS. Similar constraints have also been used for Fe at the 3g site. These constraints were used primarily to minimize the number of fit variables. The variation of the CS values for different surroundings was furthermore found to be small in the spectrum in the paramagnetic regime for Fe both at 3f and 3g, justifying the constraints used. The average hyperfine results from the fitting of spectra at 85 K are presented in Fig. 6 and Table S2.

In order to find the polar ($\theta$) and azimuthal ($\phi$) angles of the magnetic fields *versus* the principal axes of the electric field gradient (EFG) tensor at 85 K the factor $K = \frac{2\varepsilon}{QS}$ connecting the two electric quadrupole parameters QS and $\varepsilon$ can be calculated using the expression:

$$K = \frac{3\cos^2\theta - 1 + \eta\sin^2\theta\cos 2\phi}{2\sqrt{1 + \frac{\eta^2}{3}}} \quad (1)$$

where $\eta$ is the EFG asymmetry parameter and the angles $\theta$ and $\phi$ refer to the situation at 85 K. Given the magnetic state of the compounds at 85 K, QS cannot be directly measured. However, using previously reported values for $Fe_2P$,[30] QS(295 K)/QS(85 K) $\approx$ 1.15 for both Fe sites. Therefore, the values of $K$ in Fig. 6(d) has been calculated as $K \approx 1.15\frac{2\varepsilon(85K)}{QS(295K)}$. The principal $z$ axis of the EFG has been found to be in the $ab$ plane and also a negative sign for QS for both Fe sites in $Fe_2P$.[31] The calculated values of $K$ show four different regions: (i) $K \sim -0.5$ for $x$ close to

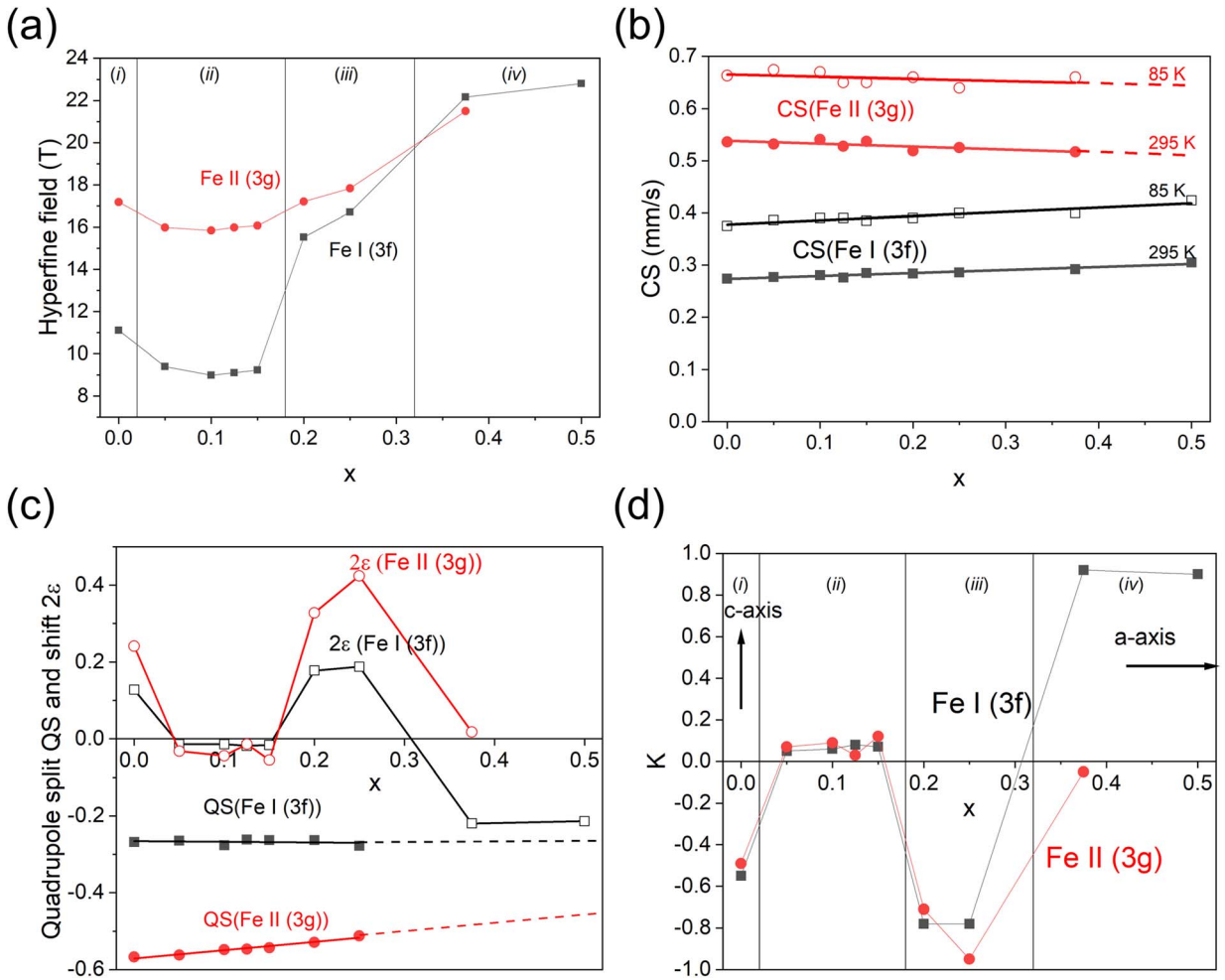


Fig. 6 (a) The average magnetic fields at 85 K for Fe at the tetrahedral 3f site and pyramidal 3g. (b) The center shift CS *versus* natural α-Fe at 295 K for $Fe_{3f}$ and $Fe_{3g}$ at 295 K and 85 K. (c) The electric quadrupole splitting QS at 295 K and electric quadrupole shift 2$\varepsilon$ at 85 K in mm $s^{-1}$. (d) The electric quadrupole ratio $K = \frac{2\varepsilon}{QS}$ at 85 K.

0, (ii) $K \sim 0$ for $x \sim 0.1$, (iii) $K \sim -0.9$ for $x \sim 0.25$ and (iv) $K \sim 0.9$ for $x \sim 0.4$–0.5 (Fig. 6(d)).

Region (i) represents the ferromagnetic structure with the magnetic moments along the *c*-axis. The polar angle is 90° with a small asymmetry parameter $\eta$, $K$ would theoretically be −0.5 as also found experimentally here. With only a slight amount of Mn and Si substitution, $B_{hf}$ drops at both crystal sites and the electric quadrupole ratio drops to zero, making the system enter region (ii).

Region (iv) represents the ferromagnetic structure with the magnetic moments along the *a*-axis. Since the orientation of the *z*-axis of the electric field gradient tensor is in the *ab*-plane, the polar angle will be unknown, as will the azimuthal angle for Fe at the tetrahedral 3f site. Experimentally $K \sim 0.9$ is observed, which can be interpreted as having the *z*-axis along the *a*-axis with small contributions from the asymmetry parameter (Eq. (1)).

Regions (ii) and (iii) are more difficult to interpret from the experimental values of $K$. The resonance lines are broad due to the different possible nn configurations of the Fe atoms. The $K$-value has therefore to be interpreted as a value averaged over all possible nn configurations. In region (ii) the average value for $K$ is close to 0 which may be interpreted as a region with varying polar and azimuthal values, a possible antiferromagnetic helical structure for the magnetic moments. The drop in the magnetic hyperfine field in region (ii) is further an indication of a more complex antiferromagnetic structure. Judging from the $B_{hf}$ results, region (iii) seems to be dominantly ferromagnetic in character.

**3.2.3 Mössbauer temperature study of the antiferromagnetic region (ii).** Here we present a temperature study of the sample with $x = 0.125$ as a representative for the antiferromagnetic region (ii). The Mössbauer spectra above 177 K could be identified as emanating from a paramagnetic phase, while spectra below 152 K were emanating from a phase where magnetic fields were acting on the Fe nucleus (Fig. 7).

The spectra in the paramagnetic regime were fitted using two doublets. In the magnetically ordered state, the spectra exhibited significant broadening due to variations in the local environment, where different numbers of neighboring Mn and

 

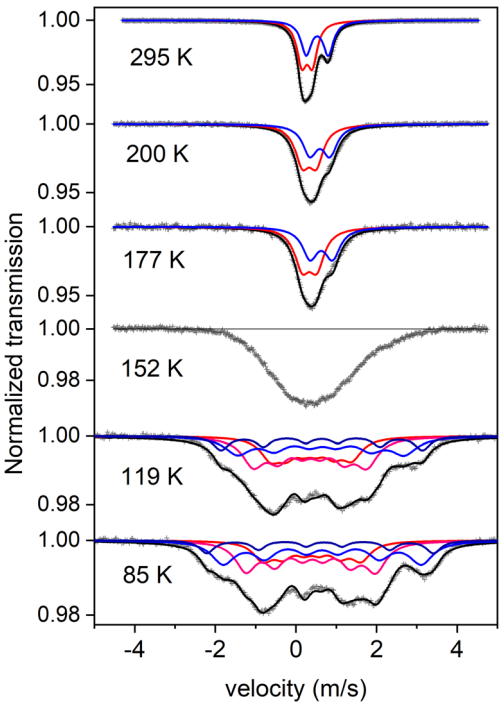


Fig. 7 Representative Mössbauer spectra of $Fe_{2-2x}Mn_{2x}P_{1-x}Si_x$ with $x = 0.125$. Blue subpatterns represent Fe at the pyramidal 3g site and red subpatterns represent Fe at the tetrahedral 3f site. A magnetic transition takes place between 152 K and 177 K.

P/Si atoms influence the magnetic field at the Fe nucleus. This broadening was approximated by four sextets, two representing Fe at the 3g site and two at the 3f site. Table S3 presents the fitted results, while Fig. 7 displays representative spectra.

It is evident that no Fe magnetic moment ordering exists above 150 K for the samples within the time scale of the Mössbauer transition $\sim 10^{-7}$ s and longer. However, the AC susceptibility results indicate slow spin dynamics with glassy behavior at ~200 K and 320 K (*cf.* Fig. 9 below); the frequency range 1.7–170 Hz corresponds to a time scale range of 1 – 100 ms. The absence of a magnetic hyperfine splitting of the $^{57}$Fe Mössbauer spectrum at temperatures $T > 150$ K can have at least two explanations. One explanation could be that the slow spin dynamics detected in the AC susceptibility measurement originate solely from the Mn magnetic moments. Another relating explanation is that the local Fe magnetic moment disappears at temperatures above the antiferromagnetic ordering temperature. The latter explanation connects to the rare case of mixed magnetism, *i.e.* the coexistence of strong and weak magnetism, discussed for hexagonal FeMn(P,Si).[5]

The AC susceptibility and Mössbauer results are consistent with the onset of magnetic ordering at ~150 K. The observed values of $\varepsilon$ (~0.00 mm s$^{-1}$) are significantly lower compared to QS (~−0.36 mm s$^{-1}$ and −0.56 mm s$^{-1}$ for Fe at the 3f and 3g sites, respectively). This suggests that a magnetic structure with moments aligned along the *c*-axis can be ruled out, as such an arrangement would yield an electric quadrupole ratio $K = \frac{2\varepsilon}{QS}$ of −0.5 (see the section on the magnetic regime above).

### 3.3 Magnetic characterisation

The temperature-dependent magnetization of the compounds studied is shown in Fig. 8(a and b). $Fe_2P$ ($x = 0$) shows a paramagnetic (PM) to ferromagnetic (FM) phase transition with a $T_C = 216(2)$ K, similar to the previously reported value.[30] A phase transition from PM to FM is also observed in the samples with $0.2 \leq x \leq 0.5$. For these four compounds, $T_C$ increases with increasing $x$, although the increase in $T_C$ levels off at higher $x$ values. Magnetic transition temperatures of $Fe_2P$-type compounds are often related to the atomic distances between

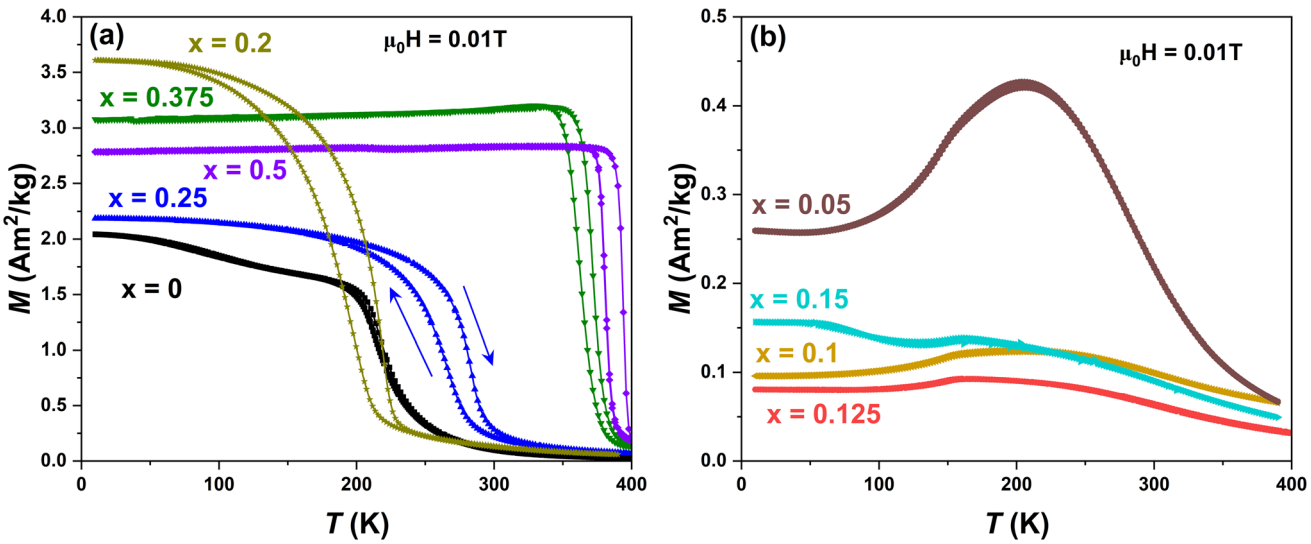


Fig. 8 Temperature dependent (a) and (b) magnetization measured under FC and FCW conditions. The direction of temperature change is indicated by arrows. To clearly distinguish the temperature dependent magnetization two different scales for the magnetization are used in (a) and (b).

Table 1 Values of $T_C$, inter-atomic distances $d_{3f-3g}$, and temperature hysteresis $\Delta T_{hys}$ of the compounds with $0.2 \leq x \leq 0.5$. The values of $T_C$ are taken from the FC magnetization *versus* temperature curves at $\mu_0 H = 0.01$ T

| $x$ | $T_C^{FC}$ (K) | $d_{3f-3g}$ (Å) | $\Delta T_{hys}$ (K) |
|---|---|---|---|
| 0 | 216 | 2.6272(4) | 20 |
| 0.2 | 196 | 2.6225(7) | 20 |
| 0.25 | 266 | 2.6523(5) | 18 |
| 0.375 | 362 | 2.6551(6) | 10 |
| 0.5 | 380 | 2.6678(4) | 14 |

the magnetic atoms situated in the 3f and 3g sites. The positions of the 3f and 3g sites and their shortest interatomic distances ($d_{3f-3g}$) were extracted from the neutron diffraction refinements. The values of $d_{3f-3g}$ and $T_C$ are shown in Table 1. It is clear that an increase of $d_{3f-3g}$ follows with an increase in $T_C$ for the four compounds with $0.2 \leq x \leq 0.5$. In $Fe_2P$, both the 3f and 3g sites are occupied by Fe, which is unlikely for the rest of the compounds. Interestingly, these four compounds exhibit thermal hysteresis ($\Delta T_{hys}$), *i.e.* a difference in the magnetic phase transition temperature between the FC and FCW magnetization curves. The presence of $\Delta T_{hys}$ is often used as an indication of a FOMT.[19]

The compounds with $0 < x \leq 0.15$ exhibit a much lower magnetization with unclear magnetic ordering (*cf.* Fig. 8(b)). The temperature-dependent magnetization curves resemble those of materials with glassy behavior. To investigate this behavior further, temperature- and frequency-dependent AC magnetic susceptibility measurements have been performed for the $x = 0.125$ compound; the results are shown in Fig. 9. The real component of the AC-susceptibility (*cf.* Fig. 9(a)) exhibits a clear frequency dependence at temperatures above 150 K. The imaginary component reveals several loss peaks (Fig. 9(b)). The presence of several frequency-dependent loss peaks is indicative of different contributions to magnetic dissipation in the temperature range of $150 \text{ K} < T < 400$ K. From a comparison of the AC susceptibility and Mössbauer results, it is concluded that

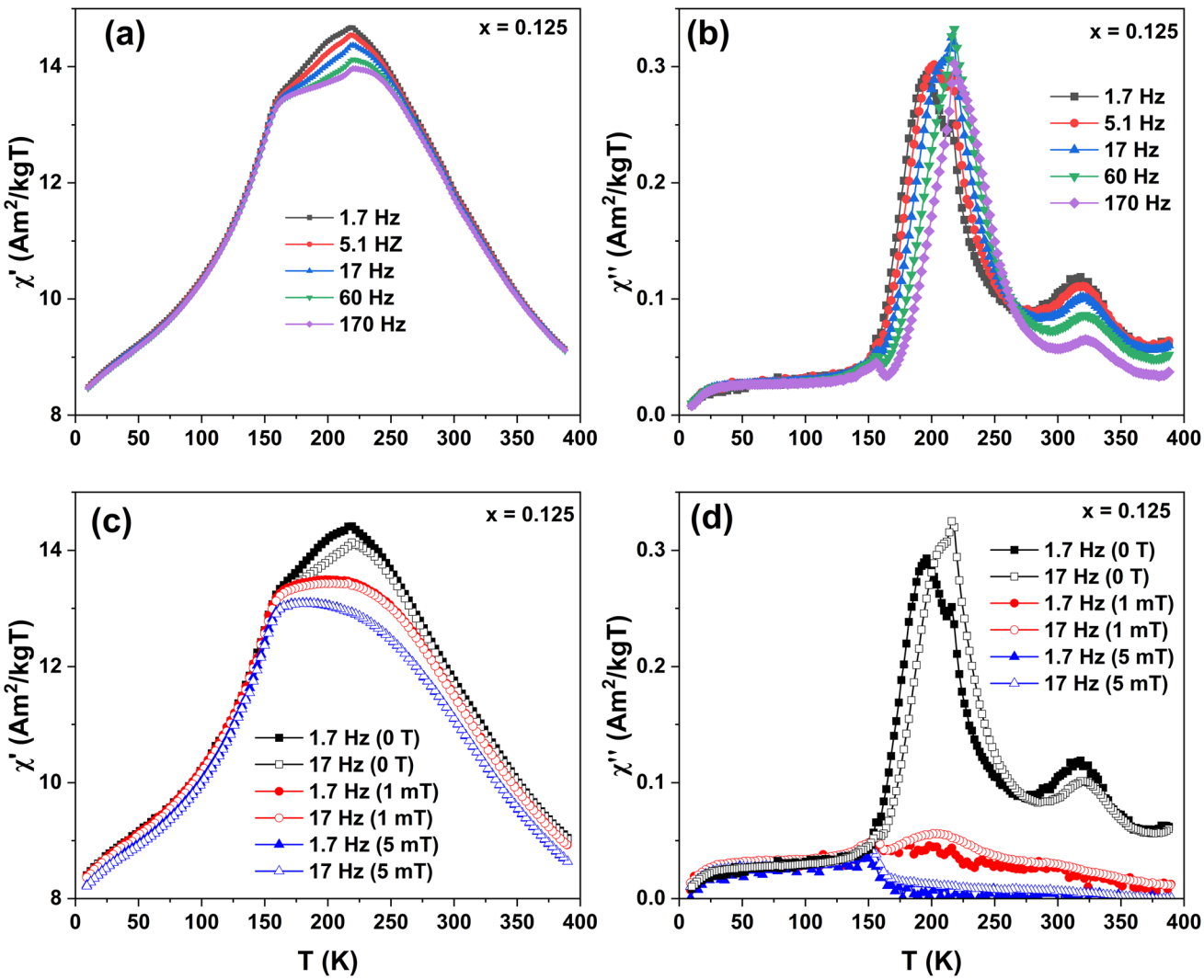


Fig. 9 Frequency and temperature dependent real and imaginary components of the AC magnetic susceptibility without applied fields (a) and (b), and with superimposed DC applied fields (c) and (d) respectively, for the $x = 0.125$ compound.

 

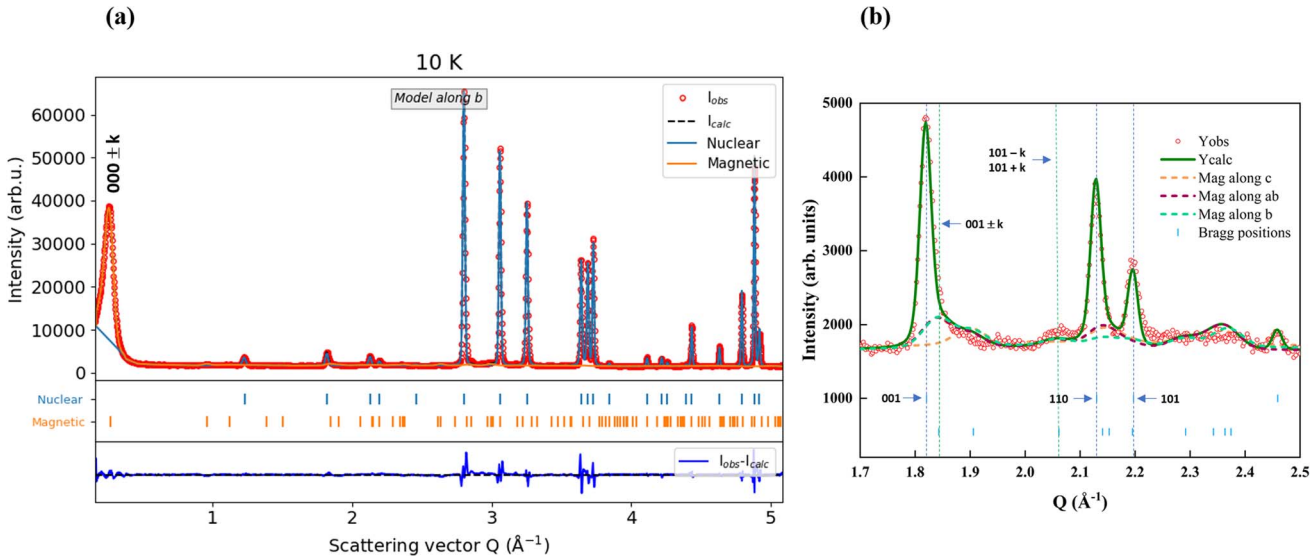


Fig. 10 (a) Observed and calculated neutron diffraction patterns of $Fe_{1.8}Mn_{0.2}P_{0.9}Si_{0.1}$ in the antiferromagnetic state, for the model with moments along *b* axis. (b) Refinement comparison of magnetic models with moments along the *c*-axis, *b*-axis, and within the *ab*-plane, shown for the enlarged magnetic satellite peaks. Dashed lines represent the magnetic contribution of each model, while the total calculated intensity for the model with moments along the *b*-axis is shown in as a green line. The *hkl* indices of the main Bragg reflections and their corresponding magnetic satellites are indicated.

the slow spin dynamics in this temperature range is solely due to the Mn magnetic moments. At the same time, the disappearance of dissipation at $T < 150$ K is in accordance with the order of AFM at low temperature involving both local Fe and Mn moments, which will be discussed below when describing the results of the magnetic structure analysis.

In order to get more insight into the glassy spin dynamics, Fig. 9(c) and (d) show AC susceptibility *versus* temperature results for fixed AC frequency (1.7 Hz and 170 Hz) along with superimposed DC magnetic fields (0–5 mT). The real component of the AC-susceptibility (*cf.* Fig. 9(c)), including its frequency dependence is suppressed by the superimposed DC magnetic field. Even more noticeable is the suppression of the imaginary component of the AC susceptibility at $T > 150$ K. In the presence of the 1 mT DC field, the loss peak at $T \approx 320$ K vanishes, while the loss peak at $T \approx 200$ K is much reduced (*cf.* Fig. 9(b)). Both loss peaks vanish in the presence of 5 mT DC field, while the relaxation behavior at $T < 150$ is unaffected by the superimposed DC magnetic fields (*cf.* Fig. 9(b)). From this it can be concluded that the spin dynamics of the antiferromagnetically ordered phase is not affected by the superimposed DC magnetic field, while the time scales of the glassy spin dynamics at $T > 150$ K are strongly DC magnetic field dependent with a shortening of the time scales with increasing DC magnetic field. A similar frequency dependent behaviour has been observed for the $x = 0.05$, 0.1, and 0.15 compounds which are discussed in SI.

To estimate the effective paramagnetic moment of the compounds ($x = 0$, 0.2, and 0.25) which show a clear PM-FM transition below 400 K, the temperature dependent inverse DC-susceptibility has been fitted to the Curie-Weiss (CW) law (Fig. S3(a) in SI).[32] The calculated effective moments are 5.96 $\mu_B$, 9.9 $\mu_B$, and 10.4 $\mu_B$ per formula unit for the $x = 0$, 0.2, and 0.25 samples, respectively. The extracted values for the $x = 0.2$, and 0.25 samples are likely overestimated, since the $x = 0.2$ sample exhibits a Griffiths phase like behaviour[33,34] and $x = 0.25$ is not

Table 2 Atomic coordinates, atomic displacement parameters and occupancy of Fe, Mn, P and Si atoms at 300 K and 10 K (antiferromagnetic state) obtained from refinements of neutron powder diffraction data for the sample $x = 0.1$. The full coordinates of the atomic sites are 3f: ($x$ 0 0), 3g: $\left(x\ 0\ \frac{1}{2}\right)$, 2c: $\left(\frac{1}{3}\ \frac{2}{3}\ 0\right)$, 1b: $\left(0\ 0\ \frac{1}{2}\right)$. For 300 K refinement, $R_{Bragg} = 2.57$, $R_{wp} = 6.58$, $R_p = 4.49$, $\chi^2 = 6.30$. For 10 K refinement, Prop. vector $q_x = 0.2204(4)$, $R_{Bragg} = 2.51$, $R_{mag} = 3.39$, $R_{wp} = 6.71$, $R_p = 4.33$, $\chi^2 = 17.2$

| | | 300 K | | | 10 K | | | |
|---|---|---|---|---|---|---|---|---|
| Atom | Site | $x$ | $B_{iso}$ (Å) | Occ | $x$ | $B_{iso}$ (Å) | Occ | $M$ ($\mu_b$) |
| FeI | 3f | 0.25601(9) | 0.43(2) | 1 | 0.2559(1) | 0.20(3) | 1 | 0.7(2) |
| FeII/MnII | 3g | 0.5935(1) | 0.43(2) | 0.8/0.2 | 0.5923(2) | 0.20(3) | 0.8/0.2 | 2.3(2) |
| PI/SiI | 2c | $\frac{1}{3}$ | 0.80(4) | 0.9/0.1 | $\frac{1}{3}$ | 0.79(6) | 0.9/0.1 | — |
| PII/SiII | 1b | 0 | 0.80(4) | 0.9/0.1 | 0 | 0.79(6) | 0.9/0.1 | — |

completely paramagnetic even at 400 K (Fig. S3(b)). Moreover, the field dependent magnetization at 400 K indicate that the samples which did not show a clear PM-FM transition (*e.g.* $x = = 0.1$ and 0.125) are also not completely paramagnetic at 400 K, as indicated in Fig. S3(b) revealing a non-linear magnetic field dependence at low fields. Therefore, among the studied compounds, in the measured temperature range, the CW law is only valid for the $x = 0$ sample, yielding a calculated effective moment of 5.96 $\mu_B$/f.u. and a Weiss temperature of 278.3 K.

### 3.4 Neutron diffraction results

$Fe_{2-2x}Mn_{2x}P_{1-x}Si_x$ ($x = 0.1$ and 0.125) samples were examined using NPD measurements at various temperatures ranging from 300 K to 10 K. The nuclear structure was determined at room temperature (300 K), while the magnetic structure was determined at 10 K. The $x = 0.125$ sample has a small amount (0.7(2)%) of the secondary phase $Fe_3Si$. The magnetic propagation vector was determined using the **k**-search program in the FullProf software. Several possible propagation vectors were obtained from the **k**-search, which were then tested to find the propagation vector that best describes the structure.

Magnetic structures for the samples $x = 0.1$ and 0.125 were determined using simulated annealing and representation analysis (SARAh). Magnetic structure refinement was performed in FullProf, utilizing the basis vectors from SARAh. The neutron diffraction patterns acquired below 150 K reveal a prominent magnetic peak, $000 \pm k$, for both samples, indicating an incommensurate antiferromagnetic (AFM) structure with a non-zero propagation vector. Some weak satellite peaks were also observed in the $Q$ range of 1.7–2.3 $Å^{-1}$. With the proposed **k**-vector, three magnetic models—moments aligned along the *b*-axis, *c*-axis, and in the *ab*-plane—were found to best fit the observed data. The primary distinction between these models lies in their fit to the weak satellite peaks, $001 \pm k$ and $101 \pm k$. Fig. 10(a) presents the observed and calculated NPD patterns for the model with moments aligned along the *b*-axis at 10 K for $x = 0.1$. The magnetic contributions of the three models, along with the total calculated intensity (nuclear and magnetic contributions) for the *b*-axis model, are shown in Fig. 10(b), here shown for $x = 0.1$. The comparison reveals that the models with moments along *ab* and *b* fit the $001 \pm k$ peak more accurately than the *c*-axis model, while the *c*-axis model fails to produce any intensity at the $101 \pm k$ peak position. Since the model with moments along the *a*-axis (not shown here) does not provide a good fit to the observed NPD pattern, it suggests that the magnetic moments are more likely to align along the *b*-axis rather than within the *ab*-plane. The $x = 0.125$ sample shows the same behavior in the NPD patterns.

For the refinement of the nuclear structure at 300 K, several profile parameters, atom occupancy, and atomic displacement parameters were refined. Fe atoms were found to occupy only the tetrahedral 3f site, while the pyramidal 3g site is occupied by the Fe and Mn atoms. These occupancies were initially refined and subsequently fixed in the final refinement. In the magnetic structure refinement at 10 K, the same parameters as those used in the 300 K refinement were refined, with atomic occupancies fixed. A symmetric Gaussian size broadening was used to fit the magnetic reflections at low temperature. Furthermore, the magnetic moment parameters and the propagation vector were refined. Table 2 shows the results of the NPD refinement at 300 K and 10 K for the $x = 0.1$ sample. The unit cell parameters at 10 K; $a = 5.8996(1)$ Å and $c = 3.4507(1)$ Å are slightly smaller than lattice parameters at 300 K; $a = 5.9156(1)$ Å and $c = 3.4553(1)$ Å. The parameter $a$ decreases continuously with decreasing temperature, while $c$ initially decreases until 150 K, after which it starts to increase down to 10 K (Fig. S4). The magnetic ordering becomes antiferromagnetic in this case, likely due to the increase in the $c/a$ ratio below 150 K.

Fig. 12 shows the proposed magnetic structure model for the $x = 0.1$ sample. The magnetic moments propagate sinusoidally along the *a*-axis with an incommensurate propagation vector of $k_x = 0.2204(4)$. The moments of atoms at the 3f and 3g sites are aligned along the *b*-axis. The magnetic moments of Fe(1) and Fe/Mn(2) atoms are 0.7(2) $\mu_B$ and 2.3(2) $\mu_B$ respectively, at 10 K. From Mössbauer spectroscopy, a sinusoidal model would give broader Mössbauer spectra due to magnetic fields ranging over a wider interval, which is not directly observed here; however the suggested model is the best from the neutron diffraction analysis.

Previous studies have shown that Fe moments at 3f sites typically have lower magnetic moments than Mn at 3g sites.[21,35,36] As the temperature decreases, $k_x$ increases for both samples ($x = 0.1$ and 0.125), with the $x = 0.125$ sample showing a larger $k_x$ (0.2254(5)) than the $x = 0.1$ sample at the same temperature (Fig. S5). The magnetic moments at the 3f and 3g sites also increase upon cooling, with the 3g site showing a slightly larger increase than the 3f site, here shown for $x = 0.1$ sample. The unusual peak shape observed for the $000 \pm k$ in the NPD pattern could be attributed to a disorder in the magnetic arrangement or multiple propagation vectors within the magnetic structure. However, incorporating additional **k**-

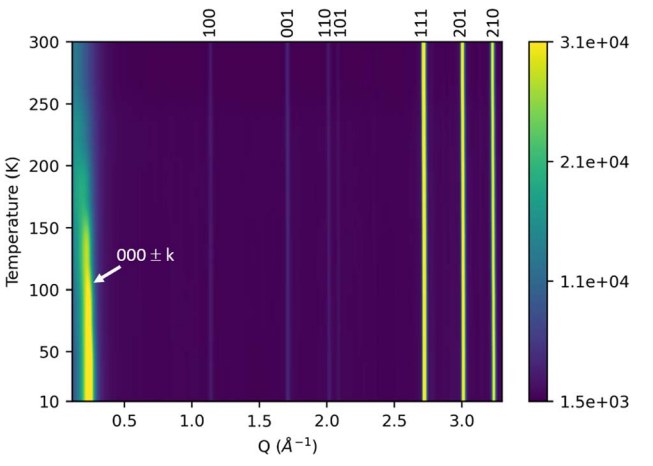


Fig. 11 Heat map of the evolution of the diffraction data for $x = 0.1$ sample in the Q region 0 to 3.3 $Å^{-1}$ on cooling. The pure magnetic reflection $000 \pm k$ ($k = (0.2203\ 0\ 0)$) has an increase in intensity below ≈150 K and shows broadening compared to the nuclear Bragg peaks in the figure.

 

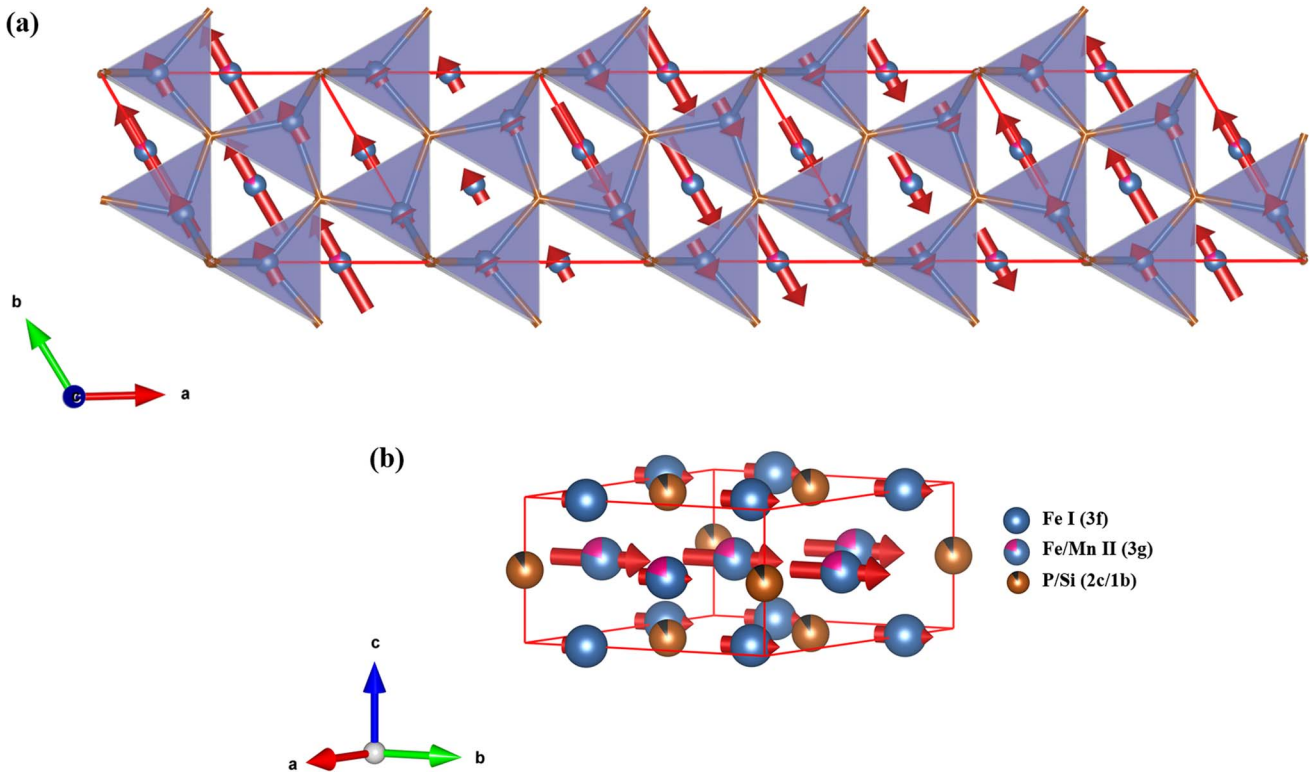


Fig. 12 (a) Magnetic structure depicting the propagation of magnetic moments along *a*-axis. Fe I atoms sitting at the 3f site are shown inside polyhedra (c) Unit cell with magnetic moments pointing along the *b*-axis.

vectors did not result in significant changes to the magnetic structure. The temperature-dependent magnetization curve for the compounds $0 < x \leq 0.15$ from magnetometry suggests that the samples are not in a purely paramagnetic state even at 300 K. The AC susceptibility measurements for the $x = 0.125$ sample reveal a glassy spin dynamics at $T > 150$ K and a possible AFM transition below 150 K. This can be correlated to the observation of a hump with slight intensity above 150 K for the $000 \pm k$ peak in the NPD data (Fig. 11) shown here for $x = 0.1$ sample, indicating short-range or fluctuating magnetic correlations which has been observed before in Fe–Mn–P–Si system.[37] With decreasing temperature, this feature evolves into a slightly broadened antiferromagnetic peak at 10 K, indicating that the system is moving from short-range to long-range order with decreasing temperature, which is not unusual.[38]

The broadness of the $000 \pm k$ peak below 150 K in the NPD pattern likely arises from the system not attaining infinite magnetic correlation even at low temperatures. It is interesting to observe that a slight substitution of Mn at one of the Fe sites alters the magnetic structure, leading to moments aligning along the *b*-axis from the *c*-axis alignment in $Fe_2P$. However, more precise information on the nature of the magnetic correlations would require a polarized neutron scattering study.

An incommensurate AFM ordering has previously been reported for the $(FeMn)_2(PSi)$ system with the composition $FeMnP_{0.75}Si_{0.25}$.[21] For this composition, Fe moments align along the *a*-axis, while Mn moments align along the *b*-axis. In $Fe_2P$-based compounds, the chemical disorder of the 3f and 3g sites and the lattice parameter ratio *c*/*a* play a crucial role in determining the ground-state magnetic order.[39]

## 4 Conclusions

The magnetic behaviour for substitutions in $Fe_2P$ has been demonstrated with neutron diffraction, Mössbauer spectroscopy and magnetometry. It is shown that $Fe_2P$ is extremely sensitive to distortions of the structure, here exemplified by substitutions.

From Mössbauer spectroscopy, a significant drop in the magnetic hyperfine field for $0.05 < x < 0.15$ as compared to $x = 0$ is observed. The drop in hyperfine field comes from the change of the magnetic structure, from ferromagnetic along the *c*-axis for $Fe_2P$, to an incommensurate antiferromagnetic structure. The magnetic hyperfine field at the tetrahedral 3f site has been found to increase by *a* factor of $\sim 2$ between $x = 0$ and $x = 0.5$. In fact, the Fe magnetic field at the tetrahedral 3f site is, at $x = 0.375$, larger than the Fe field at the pyramidal 3g site. This is in contrast to the situation in pure $Fe_2P$. These changes in the hyperfine field have a counterpart in the magnetic moments. Further Mössbauer studies are needed on samples with $x$ closer to 0 to reveal the exact nature of the antiferromagnetic structure adopted in region (ii). From magnetometry, it is observed that the samples with a small percent Mn substitution ($0.05 < x < 0.15$) exhibit glassy spin dynamics in the temperature range $150 \text{ K} < T < 400$ K, which arises solely from the Mn moments. The AC susceptibility with superimposed DC fields for a sample in this region, $x = 0.125$,

suggests an AFM behavior below 150 K. Samples with a higher substitution for Mn ($0.2 < x < 0.5$) exhibit a PM-FM transition in DC susceptibility, the same as observed for $Fe_2P$. The implication of a complex AFM structure from Mössbauer spectroscopy and magnetometry is confirmed by NPD measurements for $x = 0.1$ and 0.125 samples revealing an incommensurate AFM structure with propagation vectors $k_x = 0.2204(4)$ and 0.2254(5) respectively at 10 K. The AFM $000 \pm k$ peak for both samples exhibits a slight intensity above 150 K, suggesting the presence of short-range magnetic correlations. Furthermore, the magnetic diffraction peaks are broader than the nuclear peaks below 150 K, indicating that the system does not attain infinite antiferromagnetic correlation even at lower temperatures.

To conclude, the effect on simultaneous substitutions of Mn and Si in $Fe_2P$ to $Fe_{2-2x}Mn_{2x}P_{1-x}Si_x$ have been investigated with regard to their magnetic properties. The system show mainly ferromagnetic features with magnetic transition temperatures correlated to the interatomic distances between the two iron sites in the structure. However, a region $0.05 \leq x < 0.2$ have been found to have antiferromagnetic behavior, originating from an incommensurate magnetic structure propagating along the crystallographic $a$-axis with a propagation vector $k_x = 0.2204(4)$.

## Author contributions

Karthika K. Thilakan: conceptualization, data curation, formal analysis, investigation, methodology, visualization, writing – original draft. Sagar Ghorai: data curation, formal analysis, investigation, methodology, visualization, writing – original draft. Wei Liu: data curation, formal analysis, investigation, writing – review and editing. Lennart Häggström: conceptualization, data curation, formal analysis, investigation, methodology, visualization, writing – original draft, writing – review and editing. Fredrik Lindgren: data curation, investigation, methodology, writing – review and editing. Vladimir Pomjakushin: data curation, investigation, writing – review and editing. Premysl Beran: data curation, formal analysis, investigation, methodology, writing – review and editing. Oliver Gutfleisch: formal analysis, writing – review and editing. Peter Svedlindh: data curation, investigation, methodology, writing – review and editing. Johan Cedervall: conceptualization, data curation, formal analysis, investigation, methodology, visualization, writing – original draft, writing – review and editing.

## Conflicts of interest

There are no conflicts to declare.

## Data availability

The data that support the findings of this study are available from the corresponding author upon reasonable request. Researchers interested in accessing these datasets for replication or further studies can contact the corresponding author to request the necessary materials.

The SI contains extensive analysis of the data from Mössbauer spectroscopy and frequency-dependent AC magnetic susceptibility. See DOI: https://doi.org/10.1039/d5ta03047a.

## Acknowledgements

Financial support from the ÅForsk Foundation (grant no. 22-378), the Swedish Foundation for Strategic Research (SSF) through SwedNess (grant no. GS1715-0008) and WISE – Wallenberg Initiative Materials Science for Sustainability is gratefully acknowledged. S. G., W. L., and O. G. thankfully acknowledge the financial support of the German Research Foundation (DFG) in the framework of the Collaborative Research Centre Transregio 270 (CRC-TRR 270) and the European Union, through project CoCoMag (grant no. 101099736). This work is based on experiments performed at the Swiss spallation neutron source SINQ, Paul Scherrer Institute, Villigen, Switzerland.

## Notes and references

1 E. Brück, *J. Phys. D: Appl. Phys.*, 2005, **38**, R381.
2 V. V. Khovaylo, V. V. Rodionova, S. N. Shevyrtalov and V. Novosad, *Phys. Status Solidi B*, 2014, **251**, 2104–2113.
3 E. L. França, A. O. D. Santos, A. A. Coelho and L. M. D. Silva, *J. Magn. Magn. Mater.*, 2016, **401**, 1088–1092.
4 K. A. Gschneidner and V. K. Pecharsky, *Int. J. Refrig.*, 2008, **31**, 945–961.
5 N. H. Dung, Z. Q. Ou, L. Caron, L. Zhang, D. T. Thanh, G. A. D. Wijs, R. A. D. Groot, K. H. Buschow and E. Brück, *Adv. Energy Mater.*, 2011, **1**, 1215–1219.
6 H. Yibole, F. Guillou, L. Zhang, N. H. V. Dijk and E. Brück, *J. Phys. D: Appl. Phys.*, 2014, **47**, 075002.
7 L. Lundgren, G. Tarmohamed, O. Beckman, B. Carlsson and S. Rundqvist, *Phys. Scr.*, 1978, **17**, 39.
8 N. T. Trung, Z. Q. Ou, T. J. Gortenmulder, O. Tegus, K. H. Buschow and E. Brück, *Appl. Phys. Lett.*, 2009, **94**, 102513.
9 F. Guillou, G. Porcari, H. Yibole, N. V. Dijk and E. Brück, *Adv. Mater.*, 2014, **26**, 2671–2675.
10 D. T. C. Thanh, E. Brück, N. T. Trung, J. C. Klaasse, K. H. Buschow, Z. Q. Ou, O. Tegus and L. Caron, *J. Appl. Phys.*, 2008, **103**, 07B318.
11 M. Bacmann, J.-L. Soubeyroux, R. Barrett, D. Fruchart, R. Zach, S. Niziol and R. Fruchart, *J. Magn. Magn. Mater.*, 1994, **134**, 59–67.
12 M. Hudl, P. Nordblad, T. Björkman, O. Eriksson, L. Häggström, M. Sahlberg, Y. Andersson, E. K. Delczeg-Czirjak and L. Vitos, *Phys. Rev. B*, 2011, **83**, 134420.
13 N. H. Dung, L. Zhang, Z. Q. Ou, L. Zhao, L. V. Eijck, A. M. Mulders, M. Avdeev, E. Suard, N. H. V. Dijk and E. Brück, *Phys. Rev. B*, 2012, **86**, 045134.
14 B. Malaman, G. L. Caër, P. Delcroix, D. Fruchart, M. Bacmann and R. Fruchart, *J. Phys.: Condens. Matter*, 1996, **8**, 8653.

 

15 D. Fruchart, S. Haj-Khlifa, P. de Rango, M. Balli, R. Zach, W. Chajec, P. Fornal, J. Stanek, S. Kaprzyk and J. Tobola, *Crystals*, 2019, **9**, 37.
16 X. F. Miao, L. Caron, P. Roy, N. H. Dung, L. Zhang, W. A. Kockelmann, R. A. de Groot, N. H. van Dijk and E. Brück, *Phys. Rev. B*, 2014, **89**, 174429.
17 P. Jernberg, A. Yousif, L. Häggström and Y. Andersson, *J. Solid State Chem.*, 1984, **53**, 313–322.
18 R. Wäppling, L. Häggström, T. Ericsson, S. Devanarayanan, E. Karlsson, B. Carlsson and S. Rundqvist, *J. Solid State Chem.*, 1975, **13**, 258–271.
19 S. Ghorai, J. Cedervall, R. Clulow, S. Huang, T. Ericsson, L. Häggström, V. Shtender, E. K. Delczeg-Czirjak, L. Vitos, O. Eriksson, M. Sahlberg and P. Svedlindh, *Phys. Rev. B*, 2023, **107**, 104409.
20 T. Gottschall, K. P. Skokov, M. Fries, A. Taubel, I. Radulov, F. Scheibel, D. Benke, S. Riegg and O. Gutfleisch, *Adv. Energy Mater.*, 2019, **9**, 1901322.
21 V. Höglin, M. Hudl, L. Caron, P. Beran, M. H. Sørby, P. Nordblad, Y. Andersson and M. Sahlberg, *J. Solid State Chem.*, 2015, **221**, 240–246.
22 V. Höglin, M. Hudl, M. Sahlberg, P. Nordblad, P. Beran and Y. Andersson, *J. Solid State Chem.*, 2011, **184**, 2434–2438.
23 K. Katagiri, K. Nakamura and H. Wada, *J. Alloys Compd.*, 2013, **553**, 286–290.
24 B. Carlsson, M. Gölin and S. Rundqvist, *J. Solid State Chem.*, 1973, **8**, 57–67.
25 P. Fischer, G. Frey, M. Koch, M. Könnecke, V. Pomjakushin, J. Schefer, R. Thut, N. Schlumpf, R. Bürge, U. Greuter, S. Bondt and E. Berruyer, *Phys. B*, 2000, **276–278**, 146–147.
26 H. M. Rietveld, *J. Appl. Crystallogr.*, 1969, **2**, 65–71.
27 J. Rodriguez-Carvajal, *Phys. B*, 1993, **192**, 55–69.
28 A. Wills, *Phys. B*, 2000, **276–278**, 680–681.
29 M. J. Neish, M. P. Oxley, J. Guo, B. C. Sales, L. J. Allen and M. F. Chisholm, *Phys. Rev. Lett.*, 2015, **114**, 106101.
30 J. Cedervall, M. S. Andersson, E. K. Delczeg-Czirjak, D. Iuşan, M. Pereiro, P. Roy, T. Ericsson, L. Häggström, W. Lohstroh, H. Mutka, M. Sahlberg, P. Nordblad and P. P. Deen, *Phys. Rev. B*, 2019, **99**, 174437.
31 T. Ericsson, L. Häggström, R. Wäppling and T. Methasiri, *Phys. Scr.*, 1980, **21**, 212.
32 S. Mugiraneza and A. M. Hallas, *Commun. Phys.*, 2022, **5**, 95.
33 S. Ghorai, V. Shtender, P. Ström, R. Skini and P. Svedlindh, *J. Alloys Compd.*, 2022, **895**, 162714.
34 S. Ghorai, S. A. Ivanov, R. Skini and P. Svedlindh, *J. Phys.: Condens. Matter*, 2021, **33**, 145801.
35 Z. Q. Ou, L. Zhang, N. H. Dung, L. V. Eijck, A. M. Mulders, M. Avdeev, N. H. V. Dijk and E. Brück, *J. Magn. Magn. Mater.*, 2013, **340**, 80–85.
36 X.-F. Miao, S.-Y. Hu, F. Xu and E. Brück, *Rare Met.*, 2018, **37**, 723–733.
37 X. Miao, L. Caron, J. Cedervall, P. Gubbens, P. Dalmas de Réotier, A. Yaouanc, F. Qian, A. Wildes, H. Luetkens, A. Amato, *et al.*, *Phys. Rev. B*, 2016, **94**, 014426.
38 A. Singh, S. Mohapatra, P. Khare, N. Ganguli, A. Wildes, V. Siruguri and S. Kaushik, *Mater. Res. Express*, 2019, **6**, 066107.
39 G. Li, W. Li, S. Schönecker, X. Li, E. K. Delczeg-Czirjak, Y. O. Kvashnin, O. Eriksson, B. Johansson and L. Vitos, *Appl. Phys. Lett.*, 2014, **105**, 262405.